

Stretching Hookean ribbons

Part I: relative edge extension underlies transverse compression & buckling instability

Meng Xin and Benny Davidovitch

Physics Department, University of Massachusetts, Amherst MA 01003

The wrinkle pattern exhibited upon stretching a rectangular sheet has attracted considerable interest in the “extreme mechanics” community. Nevertheless, key aspects of this notable phenomenon remain elusive. Specifically – what is the origin of the compressive stress underlying the instability of the planar state? what is the nature of the ensuing bifurcation? how does the shape evolve from a critical, near-threshold regime to a fully-developed pattern of parallel wrinkles that permeate most of the sheet? In this paper we address some of these questions through numerical simulations and analytic study of the planar state in Hookean sheets. We show that transverse compression is a boundary effect, which originates from the relative extension of the clamped edges with respect to the transversely-contracted, compression-free bulk of the sheet, and draw analogy between this edge-induced compression and Moffatt vortices in viscous, cavity-driven flow. Next we address the instability of the planar state and show that it gives rise to a buckling pattern, localized near the clamped edges, which evolves – upon increasing the tensile load – to wrinkles that invade the uncompressed portion of the sheet. Crucially, we show that the key aspects of the process – from the formation of transversely-compressed zones, to the consequent instability of the planar state and the emergence of a wrinkle pattern – can be understood within a Hookean framework, where the only origin of nonlinear response is geometric, rather than a non-Hookean stress-strain relation.

I. INTRODUCTION

A familiar, yet quite nontrivial pattern formation phenomenon, is the parallel array of wrinkles that extend throughout a ribbon – a thin, rectangular-shaped solid sheet – upon pulling its clamped edges apart (Fig. 1A) [1, 2]. Recalling that buckling and wrinkling of a thin solid body emerge in response to compression, one may readily conclude that the visible array of wrinkles parallel to the stretching axis, \hat{x} , is due to a compressive component of the stress tensor, along the transverse axis, \hat{y} . However, while a *transverse contraction* (*i.e.* negative strain, $\varepsilon_{yy} < 0$) in response to longitudinal tension, $\sigma_{xx} \approx T > 0$, is the essence of the classical Poisson effect, the appearance of *transverse compression* (*i.e.* $\sigma_{yy} < 0$) is far less obvious. Indeed, if the pulled edges were not clamped, the whole sheet would have contracted uniformly in the transverse direction, the stress would have been perfectly uniaxial and tensile everywhere (*i.e.* $\varepsilon_{yy} \propto -\nu T$, where ν is the Poisson ratio, and $\sigma_{xx} = T$, $\sigma_{yy} = \sigma_{xy} = 0$), and the planar, unwrinkled state, would have been stable. Hence, the emergence of transverse compression is necessarily a boundary effect, which may exist only near the clamped edges. While numerical and analytical studies of the planar (unwrinkled) state did reveal the presence of zones with small transverse compression close to the clamped edges [1, 3], the physical mechanism underlying this boundary effect remains elusive.

Even more puzzling than the mere existence of transversely compressed zones in the planar state is the ensuing elastic instability. Rather than forming a buckling pattern, characterized by a thickness-independent topography that relieves the transverse compression, the stretched sheet appears to develop a highly corrugated topography, whereby the characteristic wavelength λ of

transverse undulations has been reported to be proportional to the square root of the sheet’s thickness t [2]. Elastic instabilities of thin bodies that give rise to a thickness-dependent wavelength, $\lambda \sim t^\alpha$ (with $\alpha > 0$) are often called “*wrinkling*” and are known to occur in supported sheets subjected to uniaxial compression, whereby the resistance of the attached subphase to deformation competes with the tendency of the sheet to minimize bending energy [4]. For instance, the undulation wavelength of uniaxially-compressed solid sheets that are floating on a liquid bath or attached to a compliant elastic medium scale as $\lambda \sim t$, and $\lambda \sim t^{3/4}$, respectively [5, 6]. However, why does the transverse compression of a suspended sheet give rise to a highly-curved wrinkle pattern, $\lambda \sim t^{1/2}$, whose bending energy is substantially larger than a buckling pattern ($\lambda \sim t^0$) that is also capable of relieving transverse compression?

Realizing that the observed wrinkle pattern in this system cannot be described through a standard “post-buckling” approach, in which the out-of-plane deflection of a (naturally planar) sheet is assumed to affect only slightly the planar stress, Cerda & Mahadevan (CM) proposed to address the system in a strictly distinct, “*far from threshold*” (FT) regime, $T \gg T_c$, where T_c is a threshold value, below which the compressed planar state is stable [7]. In this approach, which is based on “tension field theory” [8–12], the wrinkle pattern is assumed to be fully developed throughout the whole sheet, and cannot be described as a perturbation to the compressed planar stress, but rather to a compression-free stress field, attained by a hypothetical sheet, with finite stretching modulus and no bending modulus. The CM model inspired a multitude of experimental and theoretical works that addressed the far-from-threshold regime of wrinkle patterns in various systems of ultrathin sheets subjected to confinement by capillary effects or other forces [13, 14].

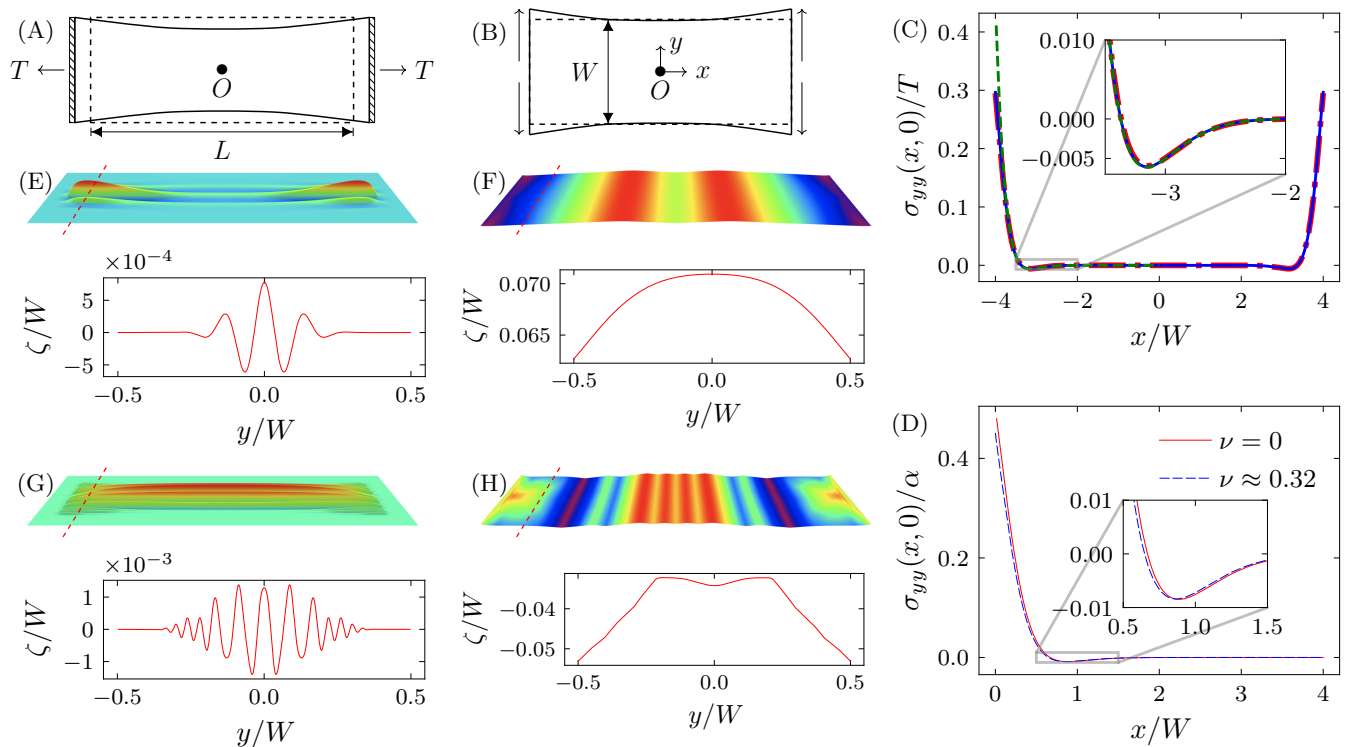


FIG. 1. (A) Schematic drawing of “model A”: a rectangular sheet with width W and length L , subjected to longitudinal tensile loads, T (*force/length*) that pull on the two short edges, $x = \pm L/2$, while the long edges are free. The short edges are clamped, such that both normal (out-of-plane) displacement, $\zeta(x = \pm L/2, y)$, and transverse (in-plane) displacement, $u_y(x = \pm L/2, y)$, vanish, and their longitudinal displacements are $u_x(x = \pm L/2, y) \approx \pm \tilde{T}L/2$. (B) Schematic drawing of “model B”: a similar sheet is subjected to uniform stretching of its two short edges, such that $\partial_y u_y(x = \pm L/2, y) = \alpha$, while $\zeta(x = \pm L/2, y) = u_x(x = \pm L/2, y) = 0$. (C) The transverse component of the planar stress, evaluated from our SE simulations along the midline, $\sigma_{yy}(x, y = 0)$, of the stretched sheet (model A, dashed-dotted red curve) and the corners-pulled sheet (model B, with $\nu_B = 0$, solid blue curve). Also plotted is the analytic solution (dashed green). The transverse stress profile exhibits a non-monotonic profile, whereby each of the edges at $x = \pm \frac{1}{2}L$ is under transverse strain $((1 - \nu_A \tilde{T})$ in model A, and $\alpha = (1 - \nu_A \tilde{T})$ in model B), and two corresponding transversely-compressed zones whose extent and distance from these edges $\sim W$. The level of the transverse compression is small, but nonetheless finite fraction of the transverse tension at the edge (the maximal compression is $-\sigma_{yy}(\pm \frac{1}{2}L \mp x_{max}, y = 0) \approx 0.005T$, where $x_{max} \approx 1.5W$). (D) A plot analogous to (C) for the corners-pulled sheet (model B) but with Poisson ratio $\nu_B = \nu_A$ (red) rather than $\nu_B = 0$ (dashed blue) exhibits an almost indistinguishable profile of the transverse stress. (E-F) The deformation $\zeta(x, y)$ of the stretched sheet (model A, in panel E) and the corners-pulled sheet (model B, in panel F) in the near-threshold regime, $\tilde{T} \approx 2\tilde{T}_c(\epsilon)$. For each model we show a topographic map and a corresponding transverse cross-section, $\zeta(x = \frac{1}{2}L - x_{max}, y)$. (G-H) Deformation patterns analogous to (E-F), but in the far-from-threshold regime, $\tilde{T} \approx 118\tilde{T}_c(\epsilon)$.

However, the ingenious proposal to focus on the FT parameter regime evades some of the basic puzzles exhibited by the system (Fig. 1A) that was the original object of the CM model. Specifically – what is the origin of transversely compressed zones underlying the instability of the planar state? why the out-of-plane deflection of the sheet does not remain localized to these near-edge zones but develops instead into a pattern of small wrinkles that permeate the uncompressed bulk?

In this paper and a subsequent one we revisit the uniaxial stretching of a Hookean ribbon-shaped sheet with clamped edges, and address the planar state, its instability, and the transition from the NT regime, $T \gtrsim T_c$, to the far from threshold regime, $T \gg T_c$. A

primary tool that we employ in our studies is numerical simulations with Surface Evolver (SE) [15], which we find to be an excellent method for finding the planar state as well as the energetic minimum of fully developed wrinkled states in the far-from-threshold regime of very thin sheets. Our rationale in focusing on Hookean elasticity (*i.e.* a linear stress-strain relationship) is twofold. First, despite the practical importance of effects associated with non-Hookean response, most notably the re-stabilization of a planar, unwrinkled state when the imposed tensile strain is sufficiently large (0.3 – 0.5 [16–22]), the Hookean response unravels the universal (*i.e.* material-independent) mechanism through which transverse compression emerges and wrinkles develop.

Second, since the instability threshold T_c vanishes rapidly with the sheet's thickness (more precisely, T_c vanishes with thickness t faster than the stretching modulus), Hookean mechanics is expected to govern for sufficiently thin sheets not only the transversely-compressed planar state and its instability, but also the fully developed wrinkle pattern in the far-from-threshold regime, $T \gg T_c$. The focus of this paper is the planar stress and the characterization of its instability. In the subsequent article we address the evolution of this instability from the near-threshold regime to a fully developed wrinkle pattern in the far-from-threshold regime.

Starting in Sec. II with numerical and analytical study of the planar state, we show that the ultimate cause of transverse compression is the extension of the clamped edges relative to the transversely contracted bulk of the sheet. We elucidate this subtlety by analyzing a specific set-up (model B in Fig. 1) and demonstrate how transverse compression in a rectangular sheet with free long edges can occur even without exerting longitudinal tensile load. In Sec. III we address the instability of the planar stress and show that it is essentially an Euler buckling, whose spatial extent is restricted to the transversely-compressed zones of the sheet. A direct corollary of this observation is that the emergence of wrinkles in this set-up, whereby the wavelength vanishes with the thickness of the sheet, does not occur at the near-threshold regime ($T \gtrsim T_c$); instead, it may only be observed in the far-from-threshold regime, $T \gg T_c$. In Sec. IV we provide evidence for the transition from near-threshold buckling to far-from-threshold wrinkling, and defer an in-depth study of the latter to a subsequent paper.

II. THE PLANAR STATE

The observation that longitudinal tension *does not* induce transverse compression if the short edges are unclamped (or alternatively if $\nu \leq 0$) suggests that the primal cause for transverse compression is neither uniaxial tension nor positive Poisson ratio, but rather a relative extension of the short edges in comparison to the bulk of the sheet. In order to elucidate this geometrical-mechanical effect, we contrast in this section the planar state of our set-up, hence called “model A” (Fig. 1A), with the planar state of another system, called “model B” (Fig. 1B), in which a relative extension of the edge is imposed directly on a rectangular sheet, with arbitrary Poisson ratio and no longitudinal tension.

A. Displacement, strain, and Hookean mechanics

Since our focus here is on small strains we express the components of the strain tensor u_{ij} through derivatives of the displacement field, whose in-plane components are

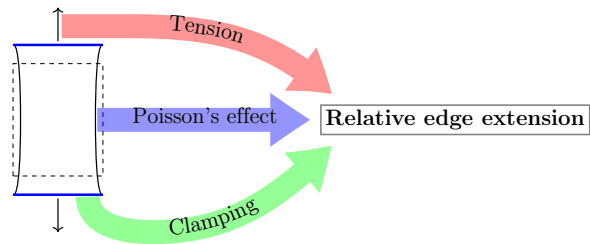


FIG. 2. The identical transverse stress profile in model A and model B indicates that the ultimate cause for a transversely compressed zone in the planar state is a relative extension of the short edge with respect to the bulk. This may be a direct outcome of pulling the short edge outward (model B) or the collective effect of imposing longitudinal tension, clamping the short edge, and positive Poisson ratio (model A).

u_x, u_y and whose out-of-plane component is ζ :

$$\begin{aligned} u_{xx} &= \partial_x u_x + \frac{1}{2}(\partial_x \zeta)^2; \quad u_{yy} = \partial_y u_y + \frac{1}{2}(\partial_y \zeta)^2; \\ u_{xy} &= \frac{1}{2}(\partial_x u_y + \partial_y u_x + \partial_y \zeta \partial_x \zeta), \end{aligned} \quad (1)$$

and invoke the Hookean stress-strain relationship [23]:

$$\begin{aligned} \sigma_{xx} &= \frac{1}{1-\nu^2} Y(u_{xx} + \nu u_{yy}); \quad \sigma_{yy} = \frac{1}{1-\nu^2} Y(u_{yy} + \nu u_{xx}); \\ \sigma_{xy} &= \frac{1}{1+\nu} Y u_{xy}. \end{aligned} \quad (2)$$

The two problems we address in this section, “model A” and “model B”, are defined below through suitable boundary conditions (BCs) on the stress tensor and the displacement field. Since we consider only small strains, we employ the standard approach of Hookean elasticity theory, and assume the BCs hold at the edges of the original, undeformed sheet, namely, the long edges $y = \pm \frac{1}{2}W$ and the short edges $x = \pm \frac{1}{2}L$. [24]

In analyzing the planar state we consider a displacement field with $\zeta = 0$. A useful tool for this analysis is the Airy potential – a scalar function $\Phi(x, y)$ such that:

$$\sigma_{yy} = \frac{\partial^2 \Phi}{\partial x^2}; \quad \sigma_{xx} = \frac{\partial^2 \Phi}{\partial y^2}; \quad \sigma_{xy} = -\frac{\partial^2 \Phi}{\partial x \partial y}. \quad (3)$$

The mechanical equilibrium equation, $\partial_j \sigma_{ij} = 0$, becomes the bi-harmonic equation for the Airy potential:

$$\nabla^4 \Phi = 0. \quad (4)$$

B. model A versus model B

The mathematical description of our original set-up (“model A”, Fig. 1A) consists of a non-homogeneous BC:

$$\int_{-\frac{W}{2}}^{\frac{W}{2}} \sigma_{xx}(x = \pm \frac{1}{2}L, y) dy = TW, \quad (5a)$$

expressing the fact that a force TW is pulling each of the short edges outward (and applies also for any $-\frac{1}{2}L \leq$

$x \leq \frac{1}{2}L$ by force balance consideration). Additionally, there are four homogeneous BCs:

$$\text{at } y = \pm \frac{1}{2}W : \quad \sigma_{yy} = \sigma_{xy} = 0 \quad (5b)$$

$$\text{at } x = \pm \frac{1}{2}L : \quad u_y = 0 \quad ; \quad \frac{\partial u_x}{\partial y} = 0 . \quad (5c)$$

The first two equations (5b) reflect the fact that the long edges are free, namely, $\sigma_{ij}n_j = 0$, where $\hat{n} = \pm\hat{y}$ is the outward normal to the long (undeformed) edges, respectively. The last two equations (5b) imply that the short edges are displaced as rigid, inextensible sticks, pulled apart along the \hat{x} axis, such that their displacement is given by $u_x = \text{Const}$ and $u_y = 0$.

With the aid of Eq. (3) the BCs (5a,5b,5c) may be converted to a set of four BCs for the Airy potential:

$$\text{at } y = \pm \frac{1}{2}W : \quad \Phi = 0 \quad (5d)$$

$$\text{and} \quad \frac{\partial \Phi}{\partial y} = \pm \frac{1}{2}TW \quad (5e)$$

$$\text{at } x = \pm \frac{1}{2}L : \quad \frac{\partial^2 \Phi}{\partial x^2} - \nu \frac{\partial^2 \Phi}{\partial y^2} = 0 \quad (5f)$$

$$\text{and} \quad \frac{\partial^3 \Phi}{\partial x^3} + (2+\nu) \frac{\partial^3 \Phi}{\partial x \partial y^2} = 0 . \quad (5g)$$

Equation (5d) follows from the first part of (5b), which implies that $\Phi(x, y = \pm \frac{1}{2}W) = C_0 + C_1x$, with arbitrary constants C_0, C_1 , upon choosing the natural gauge: $C_0 = C_1 = 0$. Integrating $\sigma_{xy}(x, y = \pm \frac{1}{2}W)$ over x one readily obtains from the second part of Eq. (5b) that $\partial_y \Phi(x, \pm \frac{1}{2}W)$ is independent on x , and Eq. (5e) is thus obtained directly from Eq. (5a), which is valid – as explained above – for any $-\frac{1}{2}L \leq x \leq \frac{1}{2}L$. Using the strain-displacement relations (1), Eq. (5f) follows directly from the first part of Eq. (5c), whereas Eq. (5g) follows from the second part of (5c) after some tedious, but straightforward algebraic manipulations.

Turning now to “model B” (Fig. 1B), we describe the BCs in analogous manner to Eqs. (5). First, the absence of exerted tension along the \hat{x} -axis implies that:

$$\int_{-\frac{W}{2}}^{\frac{W}{2}} \sigma_{xx}(x = \pm \frac{1}{2}L, y) dy = 0 , \quad (6a)$$

(as well as for any $-\frac{1}{2}L \leq x \leq \frac{1}{2}L$). Second, three BCs are identical to their homogeneous counterparts in model A:

$$\text{at } y = \pm \frac{1}{2}W : \quad \sigma_{yy} = \sigma_{xy} = 0 \quad (6b)$$

$$\text{at } x = \pm \frac{1}{2}L : \quad \frac{\partial u_x}{\partial y} = 0 , \quad (6c)$$

whereas the last BC is non-homogenous:

$$\text{at } x = \pm \frac{1}{2}L : \quad \frac{\partial u_y}{\partial y} = \alpha \quad (6d)$$

such that $\alpha > 0$ is a transverse strain imposed directly at the short edges. The conversion of the BCs (6a-6d) into BCs for the Airy potential proceeds along the same steps that led from Eqs. (5a-5c) to Eqs. (5d-5g), yielding:

$$\text{at } y = \pm \frac{1}{2}W : \quad \Phi = 0 \quad (6e)$$

$$\text{and} \quad \frac{\partial \Phi}{\partial y} = 0 \quad (6f)$$

$$\text{at } x = \pm \frac{1}{2}L : \quad \frac{\partial^2 \Phi}{\partial x^2} - \nu \frac{\partial^2 \Phi}{\partial y^2} = \alpha Y \quad (6g)$$

$$\text{and} \quad \frac{\partial^3 \Phi}{\partial x^3} + (2+\nu) \frac{\partial^3 \Phi}{\partial x \partial y^2} = 0 . \quad (6h)$$

Note that the planar stress of a Hookean sheet is determined by a purely linear problem, namely, both the strain-displacement relation (1) and the stress-strain relation (2) are given by linear equations, and consequently the stress, strain, and displacement fields for each of the two models are fully determined by solving a linear PDE (4) subjected to the corresponding BCs (Eqs. (5a-5g) for model A or Eqs. (6a-6h) for model B). Furthermore, each of the two models consists of a single non-homogeneous BC (Eq.(5a) for model A and Eq. (6d) for model B), and therefore the stress field in each model is unique up to a scale factor (and similarly the strain and displacement fields). Namely, denoting the planar stress field for model A under a given exerted longitudinal tension T by $\sigma_{ij}(x, y; T)$, and the planar stress field for model B under a given edge extension α by $\sigma_{ij}(x, y; \alpha)$, we have that:

$$\text{model A : } \sigma_{ij}(x, y; T_2) = \frac{T_2}{T_1} \sigma_{ij}(x, y; T_1)$$

$$\text{model B : } \sigma_{ij}(x, y; \alpha_2) = \frac{\alpha_2}{\alpha_1} \sigma_{ij}(x, y; \alpha_1) \quad (7)$$

C. Numerical simulations

We employ SE to study the planar state of the two models, implementing an equilateral-triangular mesh of density 6.95×10^5 (*total area/cell area*). The SE built-in “*linear-elastic*” method is adapted for computing the strain energy, and “*star-perp-sq-mean-curvature*” and “*star-gauss-curvature*” to compute bending energy.

For model A, we consider a sheet with a relatively large length-to-width ratio, $\frac{L}{W} = 8$, a Poisson ratio $\nu_A = 0.32$, and some exerted longitudinal tension T whose actual numerical value is arbitrary (see Eq. (7)). For model B, we consider a sheet with the same length-to-width ratio, $\frac{L}{W} = 8$, and Poisson ratio $\nu_B = \nu_A$ or $\nu_B = 0$. Since in model B $u_{yy} = 0$ in the bulk, we make the extension of the short edge relative to the bulk identical to model A (where $u_{yy} = 0$ at the clamped edge and $-\nu_A T/Y$ in the bulk), by choosing the edge extension parameter in model B to be $\alpha = \nu_A T/Y$.

While the longitudinal stress components, $\sigma_{xx}(x, y)$, of the two models are obviously distinct, Figs. 1c,d show that the transverse stress, $\sigma_{yy}(x, y)$ in the two models is essentially identical. Furthermore, the direct effect of

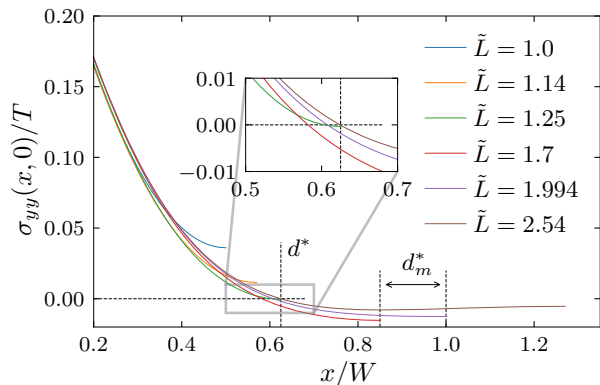


FIG. 3. Our SE simulations of the planar state in Hookean sheets with various aspect ratios, L/W , suggest the existence of a parameter regime (i) where the stress may be purely tensile and the planar state is thus stable ($\frac{L}{W} < 2d^*$); (ii) where transverse compression exists around the middle of the sheet ($2d^* < \frac{L}{W} < 2d_m^*$); and (iii) where transverse compression exists in two zones ($\frac{L}{W} > 2d_m^*$). For d^* , the numerical values extracted from our SE simulations is $d^* \approx 0.625$, whereas for d_m^* the extracted value is $d_m^* \approx 0.8 - 1.0$ (the uncertainty is a consequence of a very shallow local maximum of $\sigma_{yy}(x, 0)$.)

the Poisson ratio is negligible, as can be seen by comparing the transverse stress of model B with $\nu_B = \nu_A$ and $\nu_B = 0$. As Figs. 1c,d show, the transverse stress is positive (tensile) in the vicinity of the short edges, becoming compressive at a distance $\approx 1.5 \cdot W$ from each short edge, and remains compressive over a strip of length $\sim W$, after which it vanishes exponentially.

Our numerical solution of the planar stress in the two models indicates that the essential cause of transverse compression in a rectangular sheet is the extension of the short edge relative to the bulk. As the schematic in Fig. 2 shows, this effect can be attained directly (as is the case in model B) even for a sheet with $\nu = 0$ with no longitudinal tensile load, or indirectly – as in our original model A – by applying longitudinal tension and clamping the short edges of a sheet with positive Poisson ratio.

D. Analytical solution

1. Equivalence of model A and model B

The identity of the transverse stress components in models A and B can be understood by decomposing the Airy potential of model A into “bulk” and “edge” terms:

$$\begin{aligned} \text{model A : } \Phi(x, y) &= \Phi_b(x, y) + \Phi_e(x, y) \\ \text{where : } \Phi_b(x, y) &= \frac{1}{2}T(y^2 - 1). \end{aligned} \quad (8a)$$

If the short edges were not clamped (*i.e.* if the first part of Eq. (5c) had been replaced by $\partial_y^2 u_y = 0$, such that $u_{yy}(x = \pm \frac{1}{2}L, y)$ may be nonzero), then $\Phi_e = 0$,

and the resulting stress, associated only with Φ_b , would have been constant: $\sigma_{xx} = T, \sigma_{yy} = \sigma_{xy} = 0$. However, clamping implies that $\Phi_e(x, y) \neq 0$, since it must satisfy the nonhomogenous set of BCs:

$$\text{at } y = \pm \frac{1}{2}W : \quad \Phi_e = 0 \quad (8b)$$

$$\text{and} \quad \frac{\partial \Phi_e}{\partial y} = 0 \quad (8c)$$

$$\text{at } x = \pm \frac{1}{2}L : \quad \frac{\partial^2 \Phi_e}{\partial x^2} - \nu_A \frac{\partial^2 \Phi_e}{\partial y^2} = \nu_A T \quad (8d)$$

$$\text{and} \quad \frac{\partial^3 \Phi_e}{\partial x^3} + (2 + \nu_A) \frac{\partial^3 \Phi_e}{\partial x \partial y^2} = 0. \quad (8e)$$

Remarkably, the BCs (8b-8e) are identical to the BCs satisfied by the Airy potential $\Phi(x, y)$ of model B (6e-6h), with $\nu_B = \nu_A$, and edge extension $\alpha = \nu_A T/Y$! This observation immediately explains our numerical result: the planar stress field of the original problem (model A) is identical (up to a constant, purely uniaxial stress, $\sigma_{xx} = T, \sigma_{yy} = \sigma_{xy} = 0$) to the stress field in a sheet whose short edges are pulled outward, and no longitudinal tension.

2. The origin of transverse compression

The above discussion reveals that the origin of transverse compression in a longitudinally-stretched sheet whose short edges are clamped is the “edge-induced” potential $\Phi_e(x, y)$ in the decomposition (8a), or equivalently the Airy potential of our model B. It is thus natural to seek a solution using a basis of eigenfunctions of the bi-harmonic equation:

$$\begin{aligned} \Phi^{i,c}(x, y) &= e^{-p_i \frac{x}{W}} \cos(p_i \frac{y}{W}), \\ \Phi^{i,s}(x, y) &= e^{-p_i \frac{x}{W}} \frac{y}{W} \sin(p_i \frac{y}{W}), \end{aligned} \quad (9a)$$

where $\{p_i\}_{i=1}^{\infty}$ is a discrete set of (generally complex) eigenvalues, which must be determined through the BCs (6e-6h), and the symmetry: $\Phi(x, y) = \Phi(x, -y)$ has been exploited.

Using the basis functions (9a), we can express the Airy potential $\Phi_e(x, y)$ as:

$$\Phi_e(x, y) = \text{Re} \left\{ \sum_i C_i \cdot (\Phi^{i,c}(x, y) + A_i \Phi^{i,s}(x, y)) \right\}, \quad (9b)$$

where the sequences $\{p_i\}, \{A_i\}$, are determined by the free-edge BCs (6e,6f), yielding after some elementary manipulations:

$$p_i + \sin p_i = 0 \quad (9c)$$

$$A_i = -2 \cot \frac{p_i}{2}, \quad (9d)$$

and the sequence $\{C_i\}$ is determined from the two extended-edge BCs (6g, 6h). Remarkably, Eq. (9c) reveals two facts on whose importance we will elaborate

below: (a) All eigenvalues p_i are non-real numbers. (b) the eigenvalues p_i do not depend on the length-to-width ratio $\frac{L}{W}$, nor on the Poisson ratio ν_B .

Evaluating the sequence $\{C_i\}$ requires an inverse Laplace transform [25], which is a rather lengthy calculation, and furthermore, its implementation requires us to consider the limit of a semi-infinite sheet ($\frac{L}{W} \rightarrow \infty$, whose extended short edge is at $x = 0$). We will thus defer the details of this technical calculation to a separate publication, and report in Table I below only the values of the three eigenvalues p_i with the smallest (positive) real parts, which govern the sum (9b), together with the corresponding values of A_i and C_i .

	p_i	A_i
$i = 1$	$4.212 + 2.251j$	$0.332 + 1.78j$
$i = 2$	$10.713 + 3.103j$	$0.168 + 1.94j$
$i = 3$	$17.073 + 3.551j$	$0.111 + 1.97j$
	$\nu_B = 0.32 (\times 10^{-3})$	$\nu_B = 0 (\times 10^{-3})$
C_1	$109 - 213j$	$131 - 229j$
C_2	$-22.9 + 13.5j$	$-26.1 + 11.7j$
C_3	$8.68 - 2.84j$	$9.49 - 1.52j$

TABLE I. The values of the three leading poles (p_i), and corresponding pairs of coefficients (A_i, C_i) in the expansion, Eq. (9b), for the Airy function. Note that the pole p_i and coefficients A_i are independent on the Poisson ratio.

Figures 1C and 1D show that approximating the Airy potential through the first term in the sum (9b), *i.e.*

$$\Phi_e(x, y) \approx \text{Re}\{C_1 e^{-p_1 \frac{x}{W}} [\cos(p_1 \frac{y}{W}) - 2 \cot(\frac{p_1}{2}) \frac{y}{W} \sin(p_1 \frac{y}{W})]\}, \quad (9e)$$

matches already very well the transverse stress obtained in the numerical solution at the vicinity of the short edges of a sheet with $\frac{L}{W} = 8$. Furthermore, the analytic solution of the edge-induced Airy function $\Phi_e(x, y)$, given by Eq. (9b) with the numerical values of $\{p_i, A_i, C_i\}$ in Table 1, provides some valuable insights into the mechanism by which transverse compression develops in an elongated sheet.

- First, Table 1 indicates that the dependence on Poisson ratio, which stems only from the sequence $\{C_i\}$, is very weak. This observation, which has been noted already in our numerical analysis, substantiates the rationale illustrated in Fig. 2 – the primary cause of transverse compression is the extension of the short edges relative to the bulk, rather than the Poisson ratio of the sheet.

- Second, the unavoidable presence of transversely compressed zone in a sufficiently long sheet is a direct

consequence of the fact that all eigenvalues $\{p_i\}$, namely, roots of Eq. (9c), are complex. The implication is revealed by evaluating σ_{yy} from the approximated Airy potential (9e) along the centerline ($y = 0$) of a semi-infinite sheet:

$$\sigma_{yy}(x, y = 0) \propto e^{-p_1^{(r)} \cdot \frac{x}{W}} \cos[p_1^{(i)} \cdot \frac{x}{W} + g],$$

$$g = \tan^{-1} \left(\frac{C_1^{(i)} p_1^{(r)2} + 2C_1^{(r)} p_1^{(i)} p_1^{(r)} - C_1^{(i)} p_1^{(i)2}}{C_1^{(r)} p_1^{(i)2} + 2C_1^{(i)} p_1^{(i)} p_1^{(r)} - C_1^{(r)} p_1^{(r)2}} \right) \quad (9f)$$

where the superscripts (i) and (r) refer to the imaginary and real parts, respectively. It is evident from the first line of Eq. (9f) that the imaginary component of the root, $p_1^{(i)} \neq 0$, gives rise to negative (*i.e.* compressive) transverse stress at $-\frac{1}{2}L + d^*W < x < -\frac{1}{2}L + d_m^*W$ and $\frac{1}{2}L - d_m^*W < x < \frac{1}{2}L - d^*W$, where:

$$d^* = (\pi/2 - g)/p_1^{(i)} \approx 0.646$$

$$d_m^* = d^* + \tan^{-1}(p_1^{(i)}/p_1^{(r)})/p_1^{(i)} \approx 0.864. \quad (9g)$$

- Third, Eq. (9g), indicates that the response of a rectangular sheet whose short edges are extended relative to the bulk, can be classified into three types, depending solely on the aspect ratio, $\frac{L}{W}$:

(I) For $\frac{L}{W} < 2d^*$ there is no transverse compression. Here, the transverse stress, which is obviously tensile at the far edges ($x = \pm \frac{1}{2}L$), does not have enough room to vary significantly, hence the whole sheet is under pure (biaxial) tension.

(II) For $2d^* < \frac{L}{W} < 2d_m^*$ there is a single transversely-compressed zone located around the center of the sheet. Here, the sheet is sufficiently elongated such that the transverse stress has enough room to approach negative values away from the tensed edges, but not to overturn and decay to zero. Hence, the two compressive zones, generated by each of the tensed edges, are merged into a single one.

(III) If $\frac{L}{W} > 2d_m^*$ the sheet is long enough such that there are two transversely-compressed zones, each of them starts at a distance d^*W from a tensed edge, and extends over a length $\propto W$.

Figure 3 shows the transverse stress profile, obtained from our simulations for several representative values of the aspect ratio L/W , supporting the above classification into three regimes. We note that the actual values of d^* and d_m^* obtained from our simulations are rather close, but not identical, to the theoretical prediction, Eq. (9g). An obvious reason for this discrepancy is that the values of d^*, d_m^* , reported in Eq. (9g), are obtained from an analytic solution of the transverse stress in a

semi-infinite sheet (*i.e.* $\frac{L}{W} \rightarrow \infty$), and we may thus expect corrections of $O(\frac{W}{L})$ to this predictions. From this viewpoint, Fig. 3 indicates that those corrections to are in fact surprisingly small. Thus, while the above classification has been noted before by numerous workers (*e.g.* [16]), our analytic approach elucidates the origin of this classification through the complex values of the eigenvalues $\{p_i\}$ of the bi-harmonic equation under the BCs (6e,6e).

- Finally, we note that employing the basis functions (9a) yields a rapidly converging sequence and thereby the compact expression (9e) that describes quantitatively the stress field throughout the whole sheet. This global approach, which has been employed broadly for solving the bi-harmonic equation in viscous fluid mechanics and linear elasticity problems [25, 26] is thus advantageous to an approximation using “corner functions” [27] that does not explain the emergence of transverse compression.

3. Analogy to Moffat eddies in a “driven cavity” flow

We have seen that the existence of complex eigenvalues of the bi-harmonic equation (4) for the edge-induced Airy potential Φ_e gives rise to a non-monotonic transverse stress $\sigma_{yy} = \partial_{xx}\Phi_e$, and consequently to transversely-compressed zones. It is useful to point out an analogy between this (arguably non-intuitive) effect and a classical phenomenon in fluid mechanics, known as “Moffat eddies” [28]. Considering a class of two-dimensional (2D) viscous flows generated by the motion of rigid boundaries, Moffat showed that solutions of the bi-harmonic equation, which describes the stream function of 2D Stokes flows, may be characterized by complex eigenvalues. A notable implication of this basic observation is the emergence of eddies in the “driven-cavity” set-up, whereby a rigid plate is moving at a constant velocity, dragging the surface of a viscous fluid enclosed in a deep cavity [29] (Fig. 4). The formation of these eddies is intimately related to the complex eigenvalues that govern the stream function. The real (negative) part of the eigenvalues reflects the intuitive fact that the magnitude of the viscous stress (and consequently the speed) decays away from the driven surface, whereas the imaginary part implies that the decaying stress is nevertheless non-monotonic, and consequently an alternating direction of the velocity.

Thus, the transverse compression induced in a solid sheet by a relative extension of an edge with respect to the bulk may be viewed as an “elastic analog” of Moffat eddies in a 2D driven-cavity viscous flow, providing a notable example of the Stokes-Rayleigh analogy between the mechanical equilibrium of Hookean solids and the viscous flow of Newtonian fluids.

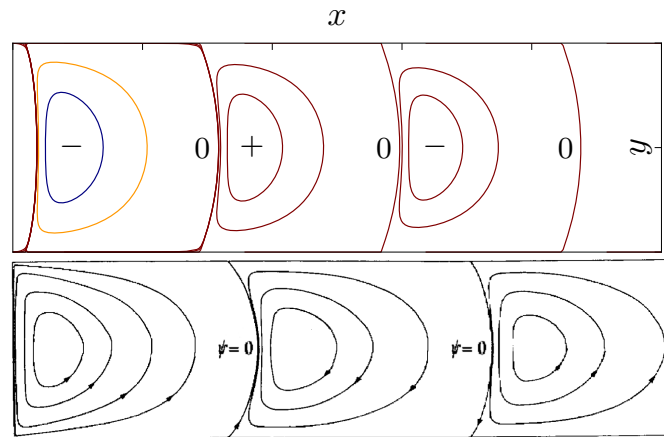


FIG. 4. Top: Contour plot of Airy potential Φ that describes the planar stress in a semi-infinite Hookean strip (9e). The symbols “+” and “-” indicate the sign of Φ . Bottom: Moffat eddies structure in a 2D Stokes flow in a driven rectangular cavity [29]. The viscous stress (and consequently the velocity field) in an incompressible Newtonian fluid is derived from a stream function that satisfies the bi-harmonic equation, similarly to the way by which the elastic stress in a solid Hookean sheet is derived from the Airy potential.

III. BUCKLING INSTABILITY

When subjected to compressive loads, slender solid bodies become unstable, “trading” a highly-energetic strain (averaged through the body’s cross section), which is penalized by the stretching modulus Y , with curvature of the body’s mid-plane, which is penalized by the bending modulus, $B \sim Yt^2$. The primary question we seek to address here is how the instability mode and the threshold value of the control parameter (longitudinal tension T in model A and edge extension α for model B) depend on the sheet thickness t .

Before studying this instability in our problem, where the planar stress is nonuniform (Figs. 1c,1d,3), it is useful to recall the basic example of a rectangular sheet under uniaxial compressive load (Fig. 5), where the planar stress is uniform and purely compressive ($\sigma_{yy} = -\sigma_0 < 0$, $\sigma_{xx} = \sigma_{xy} = 0$).

A. Instability under uniform compression

The most elementary type of an elastic instability under a uniform uniaxial compressive load, $\sigma_{yy} = -\sigma_0$, is exhibited by an unsupported rectangular sheet, of thickness t and width W , whose edges, $x = \pm\frac{1}{2}\ell$, are free (Fig. 5a). In a popular explanation of this instability, known as “Euler buckling”, the deflected state of the sheet is modeled as an Euler *elastica* – a strainless deformation that fully converts compression into out-of-plane deflection – and its bending energy ($\propto B\frac{\sigma_0}{Y}\frac{1}{W^2}$) is compared with the strain energy of the planar state ($\propto \frac{\sigma_0^2}{Y}$).

We note, however, that this common explanation is a “far from threshold” reasoning, which does not capture the physics at the vicinity of a continuous (supercritical) bifurcation. Instead, we provide here another explanation for the Euler instability, addressing it as one that emerges from a standard supercritical bifurcation, in accord with the near-threshold analysis that is the focus of the current paper.

Consider then some given value of σ_0 , and assume an undulatory deviation $\zeta(x, y) = A \cdot g_\lambda(y)$ from the planar state, where the amplitude A is *infinitesimal*, and $g_\lambda(y)$ is some function that undulates over a scale λ . Generally, $g_\lambda(y)$ is an eigenfunction of the elastic energy functional, linearized around the planar state, and for this highly symmetric problem it is simply sinusoidal. Nevertheless, we prefer to keep a more general terminology in order to highlight the commonality with our original model problem, which is far less symmetric. Such a perturbation reduces slightly the strain in the planar state: $\varepsilon_{yy} \rightarrow -\frac{\sigma_0}{Y} + C_1 \cdot (\frac{A}{\lambda})^2$, where $C_1 > 0$ is some numerical constant. For an infinitesimal A , the strain energy is reduced (from the planar-state) by a value $\propto \sigma_0 (\frac{A}{\lambda})^2$, whereas the bending energy (which is obviously zero at the planar state) is increased by a value $\propto B (\frac{A}{\lambda^2})^2$, and one readily finds that such a perturbation of the planar state becomes favorable once the compressive load exceeds a threshold, $\sigma_0^*(\lambda) \sim B/\lambda^2$. Since the wavelength λ is limited by the width W , we find that the planar state first becomes unstable to undulations at the largest possible wavelength, when the exerted compressive load exceeds a threshold value, $\sigma_c = \sigma_0^*(W)$:

$$\text{Euler buckling: } \sigma_c \sim \frac{B}{W^2} \sim Y \left(\frac{t}{W}\right)^2; \lambda \sim W. \quad (10)$$

Let us consider now two other variants of the instability under uniform, uniaxial compressive load. The first variant, known as the Winkler model and depicted in Fig. 5b, consists of a sheet attached to an elastic substrate, which penalizes vertical displacement by an energy (per area), $\frac{1}{2} K_{\text{sub}} \zeta^2$. The additional energy cost for undulations implies that, for a given λ , a planar state becomes unstable only if σ_0 exceeds an enhanced threshold value, $\sigma_0^*(\lambda) \sim B/\lambda^2 + K_{\text{sub}} \lambda^2$. Consequently, we find that the planar state first becomes unstable to undulations at a wavelength, $\lambda_c \sim (B/K_{\text{sub}})^{1/4}$, which may be $\ll W$, when the exerted compressive load exceeds a threshold value, $\sigma_c \sim \sqrt{BK_{\text{sub}}} \sim \sqrt{YK_{\text{sub}}} \cdot t$. These two features – a wavelength that exhibits strong dependence on the sheet thickness (*i.e.* $\lambda \sim t^{\beta_\lambda}$ with $\beta_\lambda > 0$) and an enhanced threshold for destabilizing a planar state (*i.e.* $\sigma_c/Y \sim t^{\beta_\sigma}$ with $\beta_\sigma < 2$) are hallmarks of wrinkling phenomena, demarcating them from the standard version of Euler buckling instability.

A second variant of instability under uniform, uniaxial compressive load, is depicted in Figs. 5c-d. Here, the amplitude is suppressed at the edges $x = \pm \frac{1}{2} \ell$, such that a shape $A \cdot \zeta_\lambda(x, y)$ that undulates over a characteristic scale λ along the compressive axis (\hat{y}), must vary also

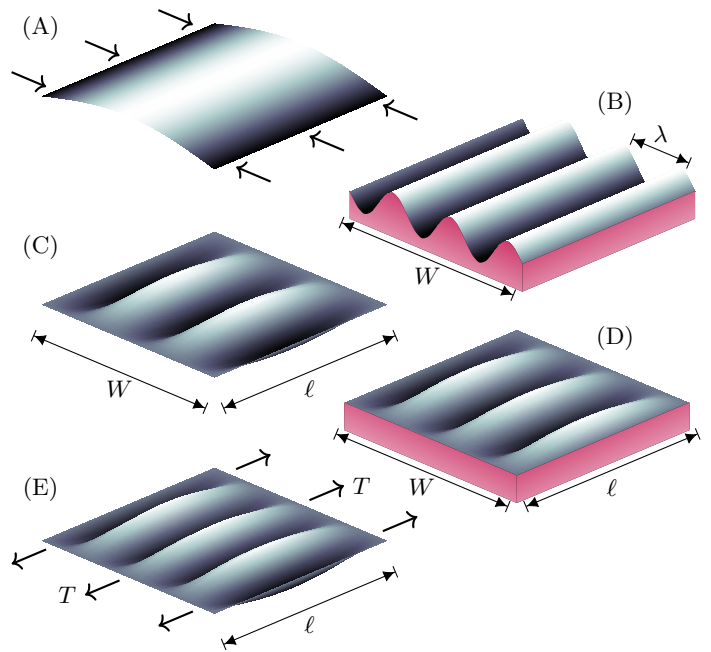


FIG. 5. A schematic of a rectangular sheet under uniaxial compressive load, $\sigma_{yy} = -\sigma_0$. (A) A classic version of the Euler buckling instability, where the edges, $x = \pm \ell/2$, are free, and the unstable mode consists of a single undulation ($\lambda \sim W$), regardless of the length ℓ . (B) Attachment to an elastic substrate (“Winkler foundation”) of stiffness K_{sub} enhances resistance to undulations and thereby the threshold σ_c , and reducing the wavelength. (C-D) If the amplitude is suppressed at the edges $x = \pm \ell/2$, the instability mode is affected by the length ℓ , such that the threshold σ_c is increased in comparison to (a) and the near-threshold undulation wavelength λ_c is decreased. For $\ell \ll W$ the near-threshold pattern consists of periodic undulations of wavelength $\lambda_c \sim \ell$. (E) The presence of longitudinal tension, $\sigma_{xx} = T$, acts as an “effective substrate” of stiffness $K \sim T/\ell^2$ [30], affecting further reduction of the wavelength and correspondingly enhancement of the threshold value σ_c .

along the \hat{x} axis, thereby being penalized also by the bending cost of the corresponding curvature, $\propto A/\ell^2$. For a given λ , a planar state becomes unstable only if the compressive load exceeds, $\sigma_0^*(\lambda) \sim B(1/\lambda^2 + \lambda^2/\ell^4)$, and if $\ell \ll W$ we find that the planar state first becomes unstable to undulations of wavelength, $\lambda_c \sim \ell$, at a threshold, $\sigma_c \sim B/\ell^2 \sim Y(\frac{t}{\ell})^2$. Furthermore, if the sheet is subjected also to a tensile load $\sigma_{xx} = T$ along the longitudinal (\hat{x}) axis (Fig. 5e), there will be yet another energetic penalty for undulations, $\sim T(\frac{A}{\ell})^2$, which is analogous to the energy implied by an actual (Winkler) substrate, $K_{\text{sub}} \propto T/\ell^2$.

Putting together the effects of a real substrate, amplitude-suppressing boundaries, and longitudinal tension, we find that, for a given wavelength λ , the planar state of a rectangular sheet under uniform compression in the transverse (\hat{y}) axis becomes unstable if the com-

pressive load σ_0 exceeds:

$$\sigma_0^*(\lambda) \sim B \frac{1}{\lambda^2} + (K_{\text{sub}} + T \frac{1}{\ell^2} + B \frac{1}{\ell^4}) \lambda^2, \quad (11a)$$

and hence the instability is characterized by a wavelength

$$\lambda_c \sim \min \left(W, \left(\frac{B}{K_{\text{sub}} + T \ell^{-2} + B \ell^{-4}} \right)^{1/4} \right) \quad (11b)$$

and occurs as the compressive load exceeds a threshold

$$\sigma_c \sim \max \left(B W^{-2}, \sqrt{B(K_{\text{sub}} + T \ell^{-2} + B \ell^{-4})} \right). \quad (11c)$$

B. Why is the instability buckling-like ?

Let us turn back now to our problem – where the transverse stress induced by the relative edge in nonuniform (Figs. 1c,1d,3), namely $\sigma_{yy}(x, y)$ varies along both \hat{x} and \hat{y} axes. One can still perform a linear stability analysis of the planar stress to infinitesimal deflections, $\zeta(x, y) = A \cdot g_\lambda(x, y)$, which undulate with a characteristic wavelength λ along the \hat{y} axis and an infinitesimal amplitude A . However, the lack of translation symmetry of the planar state implies that the eigenfunctions, $g_\lambda(x, y)$, of the corresponding (linearized) energy functional are not simply sinusoidal Fourier modes. Nevertheless, as we explain below the physical mechanisms that determine the critical wavelength λ_c and the threshold σ_c for the uniform compression problem, Eqs. (11a-11c), are analogous to those that govern the instability of the nonuniform planar stress in our problem, allowing us to gain valuable insights.

Let us consider first model B, where the magnitude $\sigma_0 \propto \alpha \cdot Y$ of the transverse compressive stress is induced directly by the edge extension parameter, α , and the stretching modulus Y . Here, there is no longitudinal tension ($T = 0$), and – since our sheet is unsupported (*i.e.* $K_{\text{sub}} = 0$) – nor there is a real substrate effect. Since the transverse compression in the planar state is limited to a narrow zone in the sheet, the compressive stress $\sigma_0^*(\lambda)$ above which a undulation of wavelength λ becomes favorable is subjected to the effect of an amplitude-suppressing boundaries discussed above (last term in Eq. 11a). However, since the length of the compressive zone is proportional to the sheet's width (*i.e.* $\ell \propto W$), the overall effect on the critical wavelength λ_c and threshold value $\sigma_c^* \propto \alpha_c Y$ is inconspicuous, and we find the scaling:

$$\text{model B: } \alpha_c \sim \frac{B}{Y W^2} \sim \left(\frac{t}{W} \right)^2 ; \quad \lambda_c \sim W. \quad (12)$$

Turning now to our original problem (model A), where the magnitude of the transverse compressive stress $\sigma_0 \propto T$, we recognize an additional contribution to $\sigma_0^*(\lambda)$, Eq. (11a), due to the energetic cost for deflection over a length $\ell \sim W$ along the tensile axis. However, since σ_0 is also proportional to the longitudinal tension T , we

find that the minimal value of T for which Eq. (11a) is satisfied is again realized when the wavelength λ is a finite, thickness-independent fraction of the sheet width, implying:

$$\text{model A: } T_c \sim \frac{B}{W^2} \sim Y \cdot \left(\frac{t}{W} \right)^2 ; \quad \lambda_c \sim W. \quad (13)$$

Thus, notwithstanding the narrowness of the compressive zone and the presence of longitudinal tension in it, inspection of Eq. (10) and Eqs. (12,13) reveals that the instability of the planar shape caused by relative edge extension exhibits the typical behavior of the classic Euler buckling instability, namely, a thickness-independent critical “wavelength” λ_c set by the sheet geometry, and a threshold load value that scales as the square power of the thickness-width ratio.

Figure 6 shows that the predicted buckling-like behavior, characterized by the scaling rules (12,13), is confirmed by our simulations. In Fig. 6a, threshold values (T_c for model A and α_c for model B) were obtained for a range of sheet thicknesses by carefully probing intervals of the control parameters (T and α , respectively), and then plotted *vs.* the aspect ratio $\frac{t}{W}$, showing an excellent agreement with the predicted scaling behavior. Apart from their identical scaling behavior, the threshold value of the dimensionless control parameter T_c/Y in model A is larger than its counterpart α_c in model B, in accord with the enhanced resistance of the former to buckling, due to the effect of longitudinal tension in the transversely compressed zone. The enhanced resistance to undulations is reflected also in the near-threshold pattern (Fig. 1e-f). While both models exhibit near threshold a buckling (*i.e.* thickness-independent undulation) pattern, such that the wavelength λ_c is a finite fraction of the width W , this fraction is smaller in model A (by a factor of $\approx \frac{1}{3}$) in comparison to its counterpart in model B.

IV. BEYOND THRESHOLD

Upon increasing the control parameter T in model A substantially above its threshold value (13), our simulations (Fig. 6c) show that the near-threshold buckling pattern undergoes two dramatic changes. First, undulations expand (along the \hat{x} axis) beyond the transversely-compressed zone of the planar state. Second, the characteristic wavelength λ becomes substantially smaller than its threshold value $\lambda_c \sim W$. For model B, the analogous process of increasing α beyond threshold (12) does lead to expansion of the deflected zone, but not to any significant reduction in the characteristic undulation wavelength.

A systematic study of this dramatic evolution from a buckling pattern to wrinkles in the (Hookean) far-from-threshold regime ($T_c \ll T \ll Y$) in model A, requires a detailed analysis of the strong effect of wrinkle formation on the stress field in the sheet, and its consequent departure from the planar stress. This non-perturbative effect,

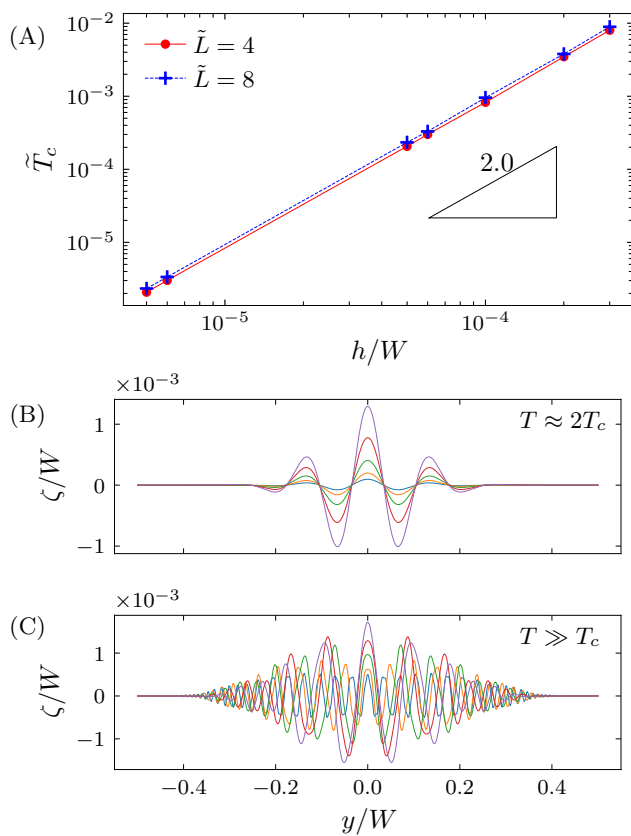


FIG. 6. (A) The instability threshold \tilde{T}_c , of a long stretched rectangular sheet with clamped edges (model A with $L = 8W$), as obtained from our SE simulations, plotted *vs.* the thickness, $\frac{t}{W}$. The threshold value is shown to be proportional to $(\frac{t}{W})^2$, with a proportionality constant that depends weakly on the aspect ratio $\frac{W}{L}$ for $L \gg W$. This result indicates that the instability is an Euler-like buckling, due to a compressed zone of width $\sim W$, where the compression is, $\sigma_{yy} \sim -T$ (see text). (B) The transverse profile of the shape (at $x \approx x_{max}$, where the compression is maximal), plotted close to threshold, indicates that the critical wavelength, λ_c , is a finite, thickness-independent fraction of the sheet width, in accord with Euler buckling instability. (C) As the exerted tension T is increased beyond T_c , the energetically-favorable wavelength λ becomes smaller (in comparison to λ_c , and develop explicit dependence on the sheet thickness. This buckling-to-wrinkling trend is consistent with a transition from near-threshold to far-from-threshold behavior envisioned in [30]. From top to bottom (looking at center $y/W = 0$), $T/T_c \approx 66, 118, 266, 1074, 4324$.

which revokes the perturbative approach underlying the near-threshold analysis in Sec. III, will be the focal point of our subsequent paper. Here, we take a more heuristic approach to rationalize the qualitative distinction between models A and B, by generalizing the analysis in the preceding section beyond the near-threshold regime.

Inspecting the considerations underlying the critical wavelength λ_c (11b), one may notice that the only way in which the planar state is explicitly affecting the wave-

length is through the length $\ell \sim W$ of the transversely-compressed zone. Assuming that even when the control parameter exceeds considerably the threshold value the wrinkle wavelength λ is affected by the stress distribution through the length ℓ of the actual compressive zone, the rule (11b) can be generalized to:

$$\lambda \sim \min \left(W, \left(\frac{B}{K_{\text{sub}} + T\ell_*^{-2} + B\ell_*^{-4}} \right)^{1/4} \right), \quad (14)$$

where ℓ_* is the *actual* length of the compressive zone (at a given, post-threshold value of the control parameter) rather its length in the planar state.

With the generalized version (14) of the wavelength rule, one may immediately notice the difference between models A and B. In the former, the presence of longitudinal tension eventually dominates the wavelength, hence:

$$\text{model A } (T \gg T_c) : \lambda \sim \left(\frac{B}{T\ell_*^{-2}} \right)^{1/4} \quad (15)$$

such that at a fixed value of T/Y , the wavelength λ vanishes with the sheet thickness, signifying a transition from buckling ($\lambda \sim W$ at $T \approx T_c$) to wrinkling ($\lambda \sim t^{1/2} \ll W$ for $T \gg T_c$). The scaling rule of Cerda & Mahadevan [30] is obtained by assuming that the transversely-compressed zone extends throughout the whole sheet, *i.e.* $\ell_* \sim L$ in Eq. (15). In contrast, for model B, the absence of longitudinal tension implies that the pattern does not undergo a similar buckling-to-wrinkling transition as the control parameter α exceeds the threshold value.

The above heuristic argument deserves a healthy dose of skepticism. Why does the transversely-compressed zone expand when the sheet is driven away from threshold? Why is it justified to approximate the energetic cost (per area) imposed on undulations by the longitudinal tension as $T(A/\ell_*)^2$? To properly address these questions one has to consider the tension-field solution of this problem, which forms the basis for far-from-threshold analysis, and will be discussed in our subsequent paper.

V. SUMMARY

Focusing on the planar stress of a Hookean, rectangular-shaped sheet under uniaxial, longitudinal tensile load, $\sigma_{xx} \approx T$, we showed that the emergence of transversely-compressed zones stems from the extension of the pulled clamped edges relative to the bulk. Specifically, we showed that an identical profile of the transverse stress is realized by directly pulling the corners transversely without longitudinal tension (Fig. 1c). This observation evinces that the classic Poisson effect, namely, “tension-induced *contraction*” of a solid sheet, must not be confused with “tension-induced *compression*” which underlies tensional wrinkling phenomena. The former is a *bulk effect*, whereby transverse *strain* ($\varepsilon_{yy} \sim -\nu T/Y$) emerges away from the edges in order to avoid compression; The latter is a *boundary effect*, which can be elim-

inated by tailoring the boundary conditions (*e.g.* unclamping the pulled edges), and hence should be referred to as “edge-induced (transverse) compression”.

Furthermore, we showed that edge-induced transverse compression stems from a non-monotonic decay of the Airy potential away from the edge, reflecting the effect of complex eigenvalues of the bi-harmonic equation, in analogy to Moffatt eddies in viscous driven cavity flow.

Finally, we showed that localized, transversely compressed zones in the planar stress give rise to *buckling* instability, with a critical wavelength λ_c proportional to the sheet width W and independent of its thickness t , and a threshold tension $T_c \sim (\frac{t}{W})^2 Y$. Both of these relations mirror the classical Euler buckling, revealing

the anticipation of Cerda & Mahadevan [30] that the commonly observed wrinkling pattern in this set-up, with a wavelength λ that vanishes with t (Fig. 1g,6c), cannot be described by a standard post-buckling theory that assumes moderate perturbation of the planar stress. A description of this wrinkling pattern through a far-from-threshold framework is the subject of a subsequent publication.

We thank F. Brau, E. Cerda, J. Chopin, P. Damman, A. Kudroli, and N. Menon for valuable discussions. This research was funded by the National Science Foundation under grant DMR 1822439. Simulations were performed in the computing cluster of Massachusetts Green High Performance Computing Center (MGHPCC).

-
- [1] N. Friedl, F. Rammerstorfer, and F. Fischer, *Computers & Structures* **78**, 185 (2000).
- [2] E. Cerda, K. Ravi-Chandar, and L. Mahadevan, *Nature* **419**, 579 (2002).
- [3] V. Nayyar, K. Ravi-Chandar, and R. Huang, *International Journal of Solids and Structures* **48**, 3471 (2011).
- [4] “buckling” is thus understood as a particular instance of “wrinkling”, where the power $\alpha = 0$.
- [5] S. T. Milner, J. F. Joanny, and P. Pincus, *Euro. Phys. Lett.* **9**, 495 (1989).
- [6] N. Bowden, S. Brittain, A. G. Evans, J. W. Hutchinson, and G. M. Whiteside, *Nature* **393**, 146 (1998).
- [7] E. Cerda and L. Mahadevan, *Phys. Rev. Lett.* **90**, 074302 (2003).
- [8] H. Wagner, *Z Flugtechn Motorluftschiffahrt* **20**, 8 (1929).
- [9] M. Stein and J. M. Hedgepeth, *Analysis of Partly Wrinkled Membranes*, Tech. Rep. (NASA, 1961).
- [10] E. H. Mansfield, *The Bending and Stretching of Plates* (Cambridge University Press, 1989).
- [11] A. C. Pipkin, *IMA J. Appl. Math.* **36**, 85 (1986).
- [12] D. J. Steigmann, *Proc. Roy. Soc. London A.* **429**, 141 (1990).
- [13] J. D. Paulsen, *Annual Review of Condensed Matter Physics* **10**, 431 (2019).
- [14] D. Vella, *Nat. Rev. Physics* **1**, 425 (2019).
- [15] K. A. Brakke, *Experimental Mathematics* **1**, 141 (1992).
- [16] V. Nayyar, K. Ravi-Chandar, and R. Huang, *International Journal of Solids and Structures* **48**, 3471 (2011).
- [17] T. J. Healey, Q. Li, and R.-B. Cheng, *J. Nonlin. Sci.* **23**, 777 (2013).
- [18] Q. Li and T. J. Healey, *J. Mech. Phys. Solids* **97**, 260 (2016), symposium on Length Scale in Solid Mechanics - Mathematical and Physical Aspects, Inst Henri Poincare, Paris, FRANCE, JUN 19-20, 2014.
- [19] A. A. Sipos and E. Feher, *Int. J. Solids. Struct.* **97-98**, 275 (2016).
- [20] C. Fu, T. Wang, F. Xu, Y. Huo, and M. Potier-Ferry, *J. Mech. Phys. Solids* **124**, 446 (2019).
- [21] T. Wang, C. Fu, F. Xu, Y. Huo, and M. Potier-Ferry, *Int. J. Eng. Sci.* **136**, 1 (2019).
- [22] A. Panaitescu, M. Xin, B. Davidovitch, J. Chopin, and A. Kudroli, *Phys. Rev. E* **100**, 053003 (2019).
- [23] L. D. Landau and E. Lifshitz, *Theory of Elasticity* (Pergamon, New York, 1986).
- [24] The error incurred by considering BCs through the undeformed, rather the deformed sheet, is a higher order in T/Y .
- [25] J. P. Benthem, *The Quarterly Journal of Mechanics and Applied Mathematics* **16**, 413 (1963).
- [26] D. A. Spence, *IMA. J. App. Math.* **30**, 107 (1983).
- [27] J. Chopin, A. Panaitescu, and A. Kudroli, *Phys. Rev. E* **98**, 043003 (2018).
- [28] H. K. Moffatt, *J. Fluid. Mech.* **18**, 1 (1964).
- [29] P. N. Shankar and M. D. Deshpande, *Annual Review of Fluid Mechanics* **32**, 93 (2000).
- [30] E. Cerda and L. Mahadevan, *Phys. Rev. Lett.* **90**, 074302 (2003).